The influence of new severe plastic deformation on microstructure, mechanical and corrosion properties of Mg-0.8Mn-0.5Ca alloy

M. Khani[1], G.R. Ebrahimi[2]*, H.R. Ezatpour[3], A. Momeni[4]

1) Department of Materials and Polymer Engineering, Hakim Sabzevari University, Sabzevar, Iran.
2) Department of Materials and Metallurgical Engineering, Faculty of Engineering, Ferdowsi University of Mashhad, Mashhad, Iran.
3) Department of Engineering Sciences, Hakim Sabzevari University, Sabzevar, Iran.
4) Department of Materials Science and Engineering, Hamedan University of Technology, Hamedan, Iran.

(Received 29 September 2020; Accepted 10 October 2021)

Abstract

In this research, the effect of accumulative extrusion bonding (AEB) on the microstructure and mechanical properties of Mg-0.8Mn-0.5Ca biocompatible alloy was investigated. The goal of this research was to develop the mechanical and corrosion properties of Mg-0.8Mn-0.5Ca alloy after ABE process as a novel severe plastic deformation process. The simulation of AEB process showed that the average effective strain per pass for channels with the internal angle of 120° is about 1.93. The average grain size was dramatically decreased from about 448.3 μm for the homogenized alloy to 1.55 μm for the 3-pass processed sample. Microstructural observations suggested a combination of continuous, discontinuous and twinning-induced dynamic recrystallization as the major mechanisms of grain refinement. Tensile and compressive strengths were improved from 150 and 205 MPa to 330 and 301 MPa after three passes of AEB, respectively indicating 2 and 1.5 times improvements, respectively. Tensile elongation decreased from 26 % for the homogenized sample to 7.5 % for the 3-pass processed sample due to the severe work-hardening, non-uniform strains and inhomogeneous microstructure produced by ABE process. Corrosion resistance in SBF solution was improved from 1.1 to 14.159 $K\Omega\ Cm^2$ after three passes of ABE due to the presence of hydroxyapatite formed on the surface of the AEBed samples.

Keywords: Mg-0.8Mn-0.5Ca alloy; Accumulative extrusion bonding; Microstructure; Mechanical properties; Corrosion.

1. Introduction

Recently, magnesium alloys have received much attention due to their high strength to weight ratio, desirable mechanical properties such as low young modulus (44 GPa) comparable to human bone marrow (17 GPa), high biocompatibility and great biodegradability [1]. These properties suggest the possibility of gradual absorption of the implant within the human body, which eliminates the costs of secondary surgery for removal of metallic implants [2]. However, the degradation rate of Mg alloys in physiological environments can be short which decreases mechanical properties in implants before restoration of the human tissue [3, 4] Eqs. (1) and (2) illustrate the anodic and cathodic reactions during the degradation of Mg alloys, respectively.

$$Mg \rightarrow Mg^{2+} + 2e^{-} \quad (1)$$

$$2H_2O + 2e^{-} \rightarrow H_2 + 2OH^{-} \quad (2)$$

According to the reactions, OH^- ions from the cathodic reaction increase the pH of the solution which stabilizes the $Mg(OH)_2$. Based on the Eq. (3), the degradation rate of Mg alloys (P_i) is obtained having the corrosion current density (i_{Corr}) [5, 6, 7].

$$P_i = 22.85\, i_{Corr} \quad (3)$$

The corrosion resistance (R_p) of the specimens can be calculated by using the electrochemical parameters, i.e. β_a, β_c and i_{Corr}, given by [5, 7]:

$$R_p = \frac{\beta_a \beta_c}{2.3(\beta_a + \beta_c) i_{corr}} \quad (4)$$

where the corrosion current density (i_{Corr}), corrosion potential (E_{Corr} V_{SCE}), Tafel cathodic slope (β_c), Tafel anodic slope (β_a) and corrosion rate (P_i) of each sample are extracted from the potentiodynamic polarization (PDP) tests.

These issues such as high degradation rate and low strength limit the comprehensive applications of magnesium implants [8]. Various techniques such as alloying [9-12], composite preparation [13-14], surface treatment [15] and use of severe plastic deformation (SPD) processes [16] have been utilized so far to overcome the drawbacks. Alloying elements must be carefully selected in the production of Mg alloys in order to avoid the release of toxic compounds in the body. Elements such as calcium (Ca), manganese (Mn), zinc (Zn), tin (Sn) and strontium (Sr) have been prioritized since they are considered as the nutrition elements [17-18]. If the Ca and Mn contents are selected correctly, it can help to improve the mechanical and corrosion properties of Mg alloys along with benefiting the human body [19-22]. Ca has been shown to be effective in grain refining of the alloy which can improve the corrosion resistance. Presence of Ca up to 0.5 wt. % has a favorable effect on grain refinement, strength increase and elongation improvement. The higher percentages result in the formation of undesirable Mg_2Ca phase, which acts as a crack source and declines the mechanical properties [23]. Mn can improve the corrosion resistance of Mg alloys by forming a passive layer on the surface. This layer prevents chloride ion diffusion into the Mg matrix. The amount of Mn for achieving the optimum of mechanical and corrosion properties in Mg alloys has been reported as 0.8 wt. % [24].

To prepare Mg-matrix composites, ceramic bioactive particles are commonly used [25-27]. Additionally, the formation of bioactive surface coatings including Ca-P [28], Si [29] and hydroxyapatite (HA) compounds [30] are proposed. As HA layer often forms on the surface grain boundaries, in fine grained alloys HA layer shows a more uniform distribution. Here, the SPD processes will be effective even on the performance of protective layers, like HA.

The SPD processes increase the grain boundary density by grain refinement, thereby improving strength and ductility. Various SPD processes have been proposed such as equal-channel angular pressing (ECAP) [31-32], multidirectional forging (MDF) [33], Dual Rolls Equal Channel Extrusion (DRECE) [34], and so on. Among these, ECAP is considered as the most effective SPD technique to produce porosity-free

bulk ultrafine-grained materials. However, some studies have reported the reduction of strength after ECAP. It has been ascribed to the formation of a soft deformation texture during the process [35-37]. The combination of ECAP and extrusion simultaneously improves the strength by grain refinement [16]. Nevertheless, the inability to perform multiple passes to achieve finer structures is one of the limitations of this method. Four mechanisms have been related to the development of ultrafine microstructure during SPD processes of Mg alloys at high temperature:

(1) Discontinuous dynamic recrystallization (DDRX): DDRX has been suggested as the main mechanism for the formation of ultra-fine grains along the primary boundaries in Mg alloys. DDRX is commonly seen in metals with low to medium stacking fault energy (SFE) such as Mg alloys. The extensive work hardening and abundant internal energy due to the aggregation of dislocations make the material prone to DDRX when strain reaches a critical value [38, 39]. The elongated grain boundaries can contribute to the nucleation of new DDRX grains by the mechanism that is called "strain-induced local grain boundary migration" (SIBM) [38-41]. In this mechanism, grain boundary locally bulges into the grain with larger stored energy and removes all dislocations in the swept volume. In the next step the dislocation-free volume is introduced as the DDRX nucleus and start to grow inside the deformed matrix. This process has been also proposed as the dominant mechanism during the hot deformation of Mg alloys. In most cases, SIBM gives rise to extensive grain boundary nucleation, which forms a necklace-like structure.

(2) Shear bands: generally, in all SPD processes, localized deformation is seen as the formation of shear bands. The flow localization in shear bands often degrades workability and may lead to premature fracture [41]. However, the strain path in SPD often alleviates the harmful effect of shear bands and therefore materials exhibit better resistance to fracture.

(3) Twinning: twin boundaries play a significant role in grain refinement of Mg alloys during SPD process. Twinning formation is controlled by temperature, alloying elements, strain rate and the primary texture in Mg alloys. It has been understood that the formation of twins is the dominant mechanism of deformation

in the early stages of SPD process in Mg alloys [43]. Twin boundaries significantly contribute to grain refinement during the first and second passes of ECAP process [5]. One idea has been the twinning dynamic recrystallization (TDRX) [44]. In this mechanism, which is only seen in Mg alloys, the mutual intersection of primary twins leads to the formation of DRX nuclei. In the next step, the boundaries surrounding the nuclei turn into random high angle grain boundaries (HAGBs) with increase in the applied strain. In fact, the nucleation phenomenon occurs by TDRX mechanism, while the growth proceeds by the continuous dynamic recrystallization.

(4) Continuous dynamic recrystallization (CDRX): observing a duplex distribution of grain size in Mg alloy. In this mechanism, the dislocation forests formed during SPD process are recovered by nucleation of new grains to decrease internal energy [45].

According to the Hall-Petch equation (5), superior strengths can be achieved by grain refinement after the SPD processes. The large strains in SPD processes refine subgrains and rotate them gradually into HAGBs. The new HAGBs act as strong obstacles against moving dislocations, leading to more work hardening and higher strengths [45].

$$\sigma_y = k_y d^{-0.5} \ (\sigma = \text{strength},\ d: \text{grain size}) \quad (5)$$

In Mg alloys, SPD is necessary; because the conventional deformation processes cannot refine the microstructure as needed. Hence, the present study presents an introduction of a new accumulative extrusion bonding (AEB) process with 120°-angle channels, for the first time in the literature. It should be mentioned that various accumulative severe plastic deformations such as accumulative rolling [47, 48] and accumulative pressing [49] have been before introduced and used for sheets. Hence, in this research, the biomedical grade Mg-0.8Mn-0.5Ca was prepared by the mechanical stir casting technique and further processed by AEB. Then the mechanical and corrosion properties of AEBed Mg-0.8Mn-0.5Ca alloy were evaluated by the standard tensile, potentio-dynamic polarization (PDP) and the hydrogen evolution immersion (HEI) tests.

2. Materials and methods

Mg ingots with 99.9 % purity, Mn flakes with 99.9 % purity and Ca with 99 % purity were used for the alloy preparation in this research. In order to produce Mg-0.8Mn-0.5Ca alloy, a total amount of 350 g Mg, 2.9 g Mn and 1.8 g Ca were inserted into an electrical furnace equipped with mechanical stirrer, heated to 750 °C and held for 15 min to melt the materials under Ar atmosphere. The casting temperature was at 750 °C. Then, the molten alloy was mixed by a mechanical stirrer at 350 rpm for 10 min under argon to produce the alloy. Finally, the melt was poured into a steel mold preheated at 400 °C. Final chemical composition was determined by inductively coupled-plasma atomic emission spectrometry (ICP-AES). The as-cast samples were homogenized under Ar atmosphere at 450 °C for 24 h. Afterwards, specimens with 80×30×15 mm^3 dimensions were prepared by CNC wire-cut machine from the homogenized ingot. The prepared specimens were preheated at 400 °C for 10 min and then inserted into the AEB die (Fig. 1) and pressed at strain rate of 1 mm/s.

Fig. 1.

The die cross section reduced from 30×15 mm^2 in the entry of channel to 15×15 mm^2 at exit and the channel angle was 45° (Fig. 2(a)). The inside and outside angles of intersection between the entry and exit channels were Φ= 120° and Ψ= 10°, respectively (Fig. 2(b)). The die was heated up to 400 °C and the mixture of graphite and refractory grease was employed as lubricant. The die was mounted on a shoe and the ram was pressed by 25-ton Zwick/Roell universal tensile/compression machine (model Z250, Sweden). After the processed samples were cooled in air. For the next passes the processed billets were cleaned by immersion in acetone for 10 min to remove remained lubricant and dust. To improve the bonding between billets, they were brushed by a wire brush to remove the oxide films and roughen the surface (Fig. 2(c)). At this stage, the surface roughness was reached Ra≈ 6.1 μm (Ra was measured by

a surface profilometer). For the next passes, the specimens were rotated 90 degrees along the horizontal axis. Both ends of samples were restrained by an instant adhesive and then inserted into the die (Fig. 2(d)).

Fig. 2.

Finite element analysis (FEA) of the introduced deformation process was studied using the Deform-3D V.5 software in order to calculate the effective strain in one pass of ECAP (ε_{ECAP}) and extrusion process ($\varepsilon_{extrusion}$) based on Eqs. (6) and (7). The average effective strain (ε_{ave}) was obtained by Eq. (8). The friction coefficient at the interface between the billet and the die was assumed to be 0.1. In addition, the magnitude of ram speed was set as 1 mm/s. 4-node linear tetrahedral elements were used to mesh the billet.

$$\varepsilon_{ECAP} = \frac{1}{\sqrt{3}}\left(2Cot\left(\frac{\Phi}{2}+\frac{\Psi}{2}\right)+\Psi\left(Cosec\left(\frac{\Phi}{2}+\frac{\Psi}{2}\right)\right)\right) \quad (6)$$

$$\varepsilon_{extrusion} = Ln\frac{A_0}{A_f} \quad (7)$$

$$\varepsilon_{ave} = \frac{\sum_{i=1}^{n}\varepsilon i}{n} \quad (8)$$

To study the mechanical properties of the AEBed samples, tensile and compression tests were carried out according to ASTM-E8 (Gauge length: 45 mm, Diameter: 9 mm as shown in Fig. 2(e)) and ASTM-E9 standards (height/diameter: 1.5), respectively. The tests were implemented using universal tensile/compression machine (model Z250, Sweden) with strain rate of 0.01 s^{-1}. Three specimens were used for each condition.

The microstructure of homogenized (before AEB) and processed (after AEB) were revealed after standard metallographic preparation method. Firstly, the specimens were cut along the extrusion transverse direction (ED-TD) and ground with 320–4000 silicon carbide (SiC) grit papers and mirror polished on the cloth using diamond compound. Then, the ground specimens were etched using a solution of 1.5 g picric acid, 25 ml ethanol, 5 ml acetic acid and 10 ml distilled water for 5-10 s. The microstructures (from center of specimens) and fracture surfaces of the samples were examined using Olympus optical microscope

(model GX51, Japan) and field emission scanning electron microscope (FESEM) TESCAN (model MIRA3, Czech Republic) equipped with energy dispersive X-ray spectroscopy (EDS). The average grain size of the samples was measured according to ASTM E112-96 standard by linear intercept method. In this standard, we counted the number of grains intercepted by test lines on a microstructure image of the specimen. The number of grain boundary intersections per unit length determined the grain size. Three specimens were used for each condition.

The biocorrosion behavior of the samples was investigated by the HEI and electrochemical tests. For hydrogen evolution test the samples with 10×10×4 mm^3 dimensions were ground by 5000 grit sand paper and placed in SBF solution for 168 h at 37±1 °C (Table 1). The volume of generated hydrogen from the specimens was measured by the burette connected to a funnel on the top of the sample and recorded with time. The PDP tests were done by immersing the mounted samples (10×10 mm^2) in SBF solution. The contact surface of samples was connected by a copper wire to Ivium-n-stat potentiostat device (model CompactStat, Netherlands) with three-electrode system. In this system the reference electrode was Ag/AgCl and platinum was the counter electrode. Primarily, the samples were exposed to open circuit potential (OCP) for 1800 s before the PDP test to achieve relative stability. The potential of working electrode was measured with respect to the reference electrode from -250 to +250 mV at scan rate of 1 mV/s. The corrosion mechanism was studied via plotting the PDP graphs and the corrosion products and corroded surface were characterized by FESEM.

Table 1. Chemical composition of SBF solution.

Reagent	**Amount**
NaCl	7.996 g
$NaHCO_3$	0.350 g
KCl	0.224 g
$K_2HPO_4.3H_2O$	0.228 g
$MgCl_2.6H_2O$	0.30 g

HCl(1.0M)	40 ml
$CaCl_2$	0.278 g
Na_2SO_4	0.071 g
Tris buffer ($(CH_2OH)_3CNH_2$)	6.057 g

3. Results and discussions

3.1. Accumulative extrusion bonding

Fig. 3(a) shows the force-displacement curves of ABEed samples at different passes. As is seen, the force increases with increment of the passes number due to the strength increase. Also, the curves present two distinct peaks during process while the first peak is related to ECAP process and the second peak indicates the start of extrusion process.

The effectiveness of grain refinement in SPD processes crucially depends on the amount of strain applied to the test specimens. Fig. 3(b) exhibits the finite element results showing the distribution and amount of average effective plastic strain in channels with 120 angle (φ) based on the Eq. (8). As the strain contour shows, there is a strain gradient in the cross-section of samples. The effective plastic strain is maximized at the outer section, where the material bears severe shear against the die surface. At the inner part, however, less friction decreases the strain by 1/3 of its value at the surface. Hence, according to the simulation results, the average effective plastic strain during one pass of AEB process is approximately about 1.93. This value is nearly two times of the average effective plastic strain reported for one pass of conventional ECAP (about 1.1) [50, 51]. Using Eq. (6), proposed for ECAP, at Φ=120° and Ψ=10°, the strain of 1 is obtained during each pass and according to Eq. (7) the lowest strain for per pass happens during simple extrusion with 2:1 ratio, i.e. about 0.7. This comparison implies that AEB with the highest strain in per pass is more capable compared to simple extrusion and conventional ECAP to refine the microstructure of metallic materials.

Fig. 3.

Fig. 3(c) shows the layers stacked after 3-pass of AEB and the morphology of their interface has been outlined in Fig. 3(d, e). As observed in Fig. 3(c), the thickness of interface between layers is about 10 μm. In most parts of the interface appropriate bonding between the layers has been obtained. The bonding of consecutive layers by AEB occurs in three stages [52]: (a) fracture of the interface layers by the severe deformation and their elongation alongside the extrusion direction, (b) extrusion of the underlying materials through widening cracks in the surface layers from both sides of the interface and (c) formation of atom-to-atom bonds between the layers.

In the entry channel, the bonding between the surfaces occurs to some extent due to the pressure of die walls. Then, the bonding is strengthened during passing through the exit channel. The number of layers in AEB process (L) is obtained by:

$$L = 2^{n-1} \tag{9}$$

where, n is the pass number. In parallel to increase in the number of layers (L), the thickness of layers (T) reduces as follows:

$$T = \frac{T_0}{2^{n-1}} \tag{10}$$

where, T_0 is the thickness of initial sample. Taking n= 3 (number of passes in this research) and T_0= 15 mm (the initial thickness), L and T can be calculated as 4 and 3.75 mm, respectively which is in agreement with Fig. 3(c).

3.2. Microstructure characterizations

Fig. 4 displays the microstructure and grain size of different sections of the AEBed samples. The micrographs clearly show the development of microstructure in different stages of the process including initial microstructure (Fig. 4(a)), before ECAP (Fig. 4(b)), after ECAP (Fig. 4(c)) and after extrusion (Fig. 4(d)). A comparison between Figs. 4(c) and 4(d) reveals that the grains have been subjected to larger strain

and are evidently more elongated near the internal angle of channels. This indicates that there is a gradient of strain in the ECAP stage, so that the strain rises from the bottom to the top of channel. Based on the observations in Fig. 4, the first pass of AEB can refine the average grain size of Mg-0.8Mn-0.5Ca alloy from 448 μm at the start of process to 24.26 μm at the end; this is about 95 % reduction in grain size. Fig. 4(b, c) shows that very fine new grains have nucleated on the prior grain boundaries at severe deformed zones while the nucleation of new grains has not begun outside the zones. It appears that dynamic recrystallization is the main mechanism for the formation of fine grains in the ECAP region. In agreement with the observations in Fig. 4(b, c) in ABEed Mg alloy, other microstructural studies on Mg alloys under SPD have indicated that larger strains localized in the shear bands boosts the kinetics of DRX [53-55]. The pioneering recovery and recrystallization in shear bands play essential roles in grain refinement during ECAP [56].

Fig. 4.

Fig. 5(a) evidences the bulged grain boundaries through SIBM in the lower part of ECAP region. Fig. 5(b) supports the idea of SIBM, showing the necklace structure of DDRXed grains alongside the primary grain boundaries in the ECAP region. Fig. 5(c, d) illustrates the formation of some twin boundaries in the ECAP region in the studied material. As arrows point to the appearance of twins inside the old deformed grains and their clear intersection fortifies the idea that they may work in favor of recrystallization by the TDRX mechanism [44]. In addition to the nucleation and growth as that happens during DDRX (Fig. 5(a)), they are convinced that the formation of the new grains may be through the gradual transformation of low-angle boundaries to high-angle ones by the absorption of more dislocations with increase in the applied strain. This process can also accomplish the nucleation by TDRX mechanism, as discussed before. CDRX is intrinsically a gradual process with strain and takes part in grain refinement by increase in the

ECAP pass number [55]. Eventually, the primary grains are transformed to finer grains during the successive passes, but no change occurs in the primary dynamic recrystallized grains.

Fig. 5.

Fig. 6 displays the trend of grain size reduction after one, two and three passes of AEB. As seen, the average grain size has gradually decreased from about 448 μm in the homogenized sample (Fig. 6(a)) to 49, 12.5 and 1.5 μm after the first, second and third passes of AEB (Figs. 6(b-d)). The gradual decrease in the surface fraction of recrystallized regions and average grain size strengthen the idea that CDRX plays a major role in the recrystallization behavior of AEBed Mg-0.8Mn-0.5Ca.

Fig. 6.

3.3. Mechanical properties

Fig. 7 exhibits the tensile and compressive stress-strain curves of the homogenized and AEBed samples. It is evident that by increasing the passes number, the compressive and tensile strengths improve, while the compressive and tensile elongations decrease. The tensile and compressive strengths of the homogenized alloy were 150 and 205 MPa, respectively. After the third pass, the tensile and compressive strengths enhance to 330 and 301 MPa that represent 2 and 1.5 times increase, respectively (Table 2). The strength improvement can be attributed to the considerable grain refinement observed in Fig. 6 [56-58]. As mentioned before, the average grain size of the homogenized sample and after three passes of ABE was 448 μm and 1.5 μm, respectively.

Fig. 7.

Table 2. Mechanical characteristics of the investigated Mg-Mn-Ca alloy at different conditions.

	Compression properties	**Tensile properties**

Sample	YS (MPa)	UTS (MPa)	Failure strain (%)	YS (MPa)	UTS (MPa)	Failure strain (%)
Homogenized	50	205	36.2	60	150	28
1-pass ABE	70	240	20..5	105	240	14
2-pass ABE	115	280	12	130	275	5.5
3-pass ABE	140	301	15.6	176	330	8

The results also show that the elongation of processed samples decreases as their strength rises with increased pass number (Table 2). The reduction in elongation is partly ascribed to the heavily work hardened microstructure, the large amount of non-uniform strains induced during process and inhomogeneous microstructure [59, 60]. The considerable increase in the number of dislocations rises their interactions and form a lot of dislocation tangles. The density of dislocations and dislocation tangles increasingly increase with the effective strain and passes number. Hence, the decreased elongation in AEBed samples is related with the short mean-free path of dislocations in the highly work hardened matrix [46].

Fig. 8 shows SEM micrographs from the fractured surface of tensile samples. As shown in Fig. 8(a), the homogenized sample shows a typical ductile fracture with deep dimples. The ductile fracture begins with the nucleation of dimples at locations with stress concentration or around inclusions [61]. Afterwards, the dimples grow and coalesce to form micro-cracks. The growth of micro-cracks and cutting the cross-section are the next steps. Finally, the metal-to-metal contact area becomes too small to support the load and fracture occurs. After one-pass of AEB the fracture surface shows refined dimples (Fig. 8(b)). Finer dimples in one-pass processed samples is consistent with its lower ductility. This is because the size of dimples is an index to the level of ductility, so that the larger dimples, the higher ductility will be. Hence, comparison of dimples size in Figs. 8(a) and 8(b) implies that ductility has decreased after one pass of AEB. Fig. 8(c, d) shows that after the second and third passes dimples size becomes finer and elongated dimples are observed. The shallow and narrow elongated dimples indicate that the failure mode has changed to shear ductile rupture. In addition, the appearance of shear lips and facets, shown by arrows,

imply that a combined mode of ductile-cleavage governs the fracture morphology of 2-pass and 3-pass processed samples. These observations well agree with the reduced elongation in Fig. 7.

Fig. 8.

3.4. Biocorrosion behavior

Fig. 9(a) demonstrates the potentio-dynamic polarization (PDP) curves of the homogenized specimen and the samples processed by one, two and three AEB passes in the SBF solution. In the early stages of the test, the anodic polarization curves show a high corrosion rate. By reaching the passive region, the anodic polarization curves are stabilized. The passive region of the anodic polarization curves may be related to the formation of corrosion products that act as the protective coating on the material surface [6, 7]. As shown in Fig. 9(a), by increase in the number of AEB passes, the rate of anodic and cathodic reactions has declined, so that the curves are shifted to the upper left side.

Fig. 9.

Table 3 reports electrochemical parameters of different samples in SBF solution. The current density of the homogenized sample is 63$\frac{\mu A}{Cm^2}$, which is much higher than that of the three passes processed sample (3.63$\frac{\boldsymbol{\mu A}}{\boldsymbol{Cm^2}}$). Based on the Eq. (3), the corrosion rate decreases from 1.439 for homogenized sample to 0.082 mm/year for 3-pass ABEed sample and the corrosion resistance (R_p in Eq. (4)) improves from 1.1 kΩ for the homogenized sample to 14.159 kΩ for the 3-pass processed sample.

Table 3. Electrochemical parameters of different samples in SBF solution.

Sample	**Corrosion potential** $\mathbf{E_{Corr}(mV_{SCE})}$	**Current density** $\mathbf{i_{Corr}(\frac{\mu A}{Cm^2})}$	**Cathodic slope** $\mathbf{\beta_c(\frac{mV}{Dec_{SCE}})}$	**Anodic slope** $\mathbf{\beta_a(\frac{mV}{Dec_{SCE}})}$	**Polarization resistance** $\mathbf{R_p(K\Omega\ Cm^2)}$	**Corrosion rate** $\mathbf{P_i(\frac{mm}{year})}$

Mg Alloy Homogenized	-1.533	63	0.378	0.274	1.1	1.4395
1-pass ABE	-1.5012	13.20	0.253	0.258	4.234	0.3016
3-pass ABE	-1.415	3.6308	0.257	0.219	14.159	0.08296

By increase in the number of passes, the current density and electrochemical potential decrease which indicate the material becomes nobler (reducing the corrosion rate). This improvement can be related to the corresponding changes in the grain size of material by AEB. By increasing the number of the passes of the process, the grain size decreases and this structural modification enhances the corrosion resistance. Improvement of corrosion resistance by the decrease in the grain size can be attributed to (1) the decrease in the volume increase-induced stresses as a result of lower damage of protective layer and (2) formation of more adhesive and strong protective layer on the sample surface [25, 60]. However, in the ABEed samples, the formation of the hydroxyapatite (HA) protective layer on the surface of the Mg-Mn-Ca alloy causes a significant improvement of the corrosion resistance.

During the HEI test the following reaction happens [19]:

$$Mg + 2H_2O \rightarrow Mg(OH)_2 + H_2 \quad (11)$$

Fig. 9(b) exhibits the HE tests results of different samples immersed in SBF solution for 168 h. The aggregation of corrosion products on the surface gradually reduces the rate of HE. The volume of generated hydrogen increases with increase in the immersion time. This is attributed to the destruction of the corrosion products and penetration of the corrosive solution to the surface underneath. The results imply that by increasing the number of AEB passes, the volume of generated hydrogen declines.

The morphology of corroded surface and the composition of the corrosion products of different samples, immersed in SBF solution for 7 days were investigated by FESEM (Fig. 9(c-e)). As shown in Fig. 9(c), severe homogeneous corrosion has occurred in the homogenized sample. The corroded surface can be divided into two zones, suggesting various corrosion mechanisms. The first zones are deep pits indicating

the severe pitting corrosion. Lack of corrosion products around the pits indicate that they act as the deep channels for the penetration of solution to the surface. The second zones are smooth and low corroded areas with a network-like morphology. Comparing the SEM micrographs helps to deduce that the depth of corrosion pits is much smaller in AEBed samples than in the homogenized sample. Also, the dense layer of hydroxyapatite in fine-grained (especially 2-pass and 3-pass processed) samples seems to be responsible for slowing down the HE (Fig. 9(e)). For the homogenized microstructure, the corrosion product layer is loose which is easily formed in vicinity of grain boundaries. Generally, the high density of grain boundaries is associated with the change of the structure discontinuity between the Mg matrix and layer which is beneficial for the formation of dense product layer [50, 62]. The precipitated network-like film on the surface of the AEBed samples has calcium phosphate compounds such as hydroxyapatite, which is formed due to the reaction of phosphate and calcium ions with hydroxide ions in the SBF solution. In addition, the pits in AEBed samples are covered with corrosion products. The corroded surface of AEBed samples contains numerous micro-cracks, which are nearly absent in the surface of the homogenized sample.

Fig. 9.

Table 4 compares the corrosion rate of the Mg-0.8Mn-0.5Ca alloy processed by ABE with other results reported in literature which indicates a considerable improvement in corrosion resistance in the processed samples in the present work.

Table 4. Comparison of the lowest corrosion rate of the Mg-0.8Zn-0.5Ca alloy processed by ABE with reported values for different alloys in the literature.

Alloy	State	Solution	Corrosion rate (mm/y)	Ref
Mg-2Zn-Ca-0.5Mn	As-cast	Hank's	1.58	[63]
Mg-2Zn-Ca-0.5Mn-1.3Ce	As-cast	Hank's	1.34	[63]
Mg–2Ca–0.5Mn–2Zn	As-cast	SBF	1.78	[4]

Mg–2Ca–0.5Mn–4Zn	As-cast	SBF	2.27	[4]
Mg–2Ca–0.5Mn–7Zn	As-cast	SBF	3.98	[4]
Mg-Zn-1.5-Ca-1.1Mn	As-cast	Hank's	1.40	[64]
6h-coated Mg-2Zn-Ca-0.5Mn-1.3Ce	As-cast	Hank's	1.29	[65]
ZK60	As-extruded	Hank's	0.32	[66]
Annealed Mg-Zn-Ca	SPD (HPT)	SBF	1.30	[62]
Mg-0.8Mn-0.5Ca	ABE	SBF	0.08	Present work

4. Conclusions

In this study, the effect of 1-3 passes of accumulative extrusion bonding (AEB) through 120°-angle channels at 400 °C on the microstructure, mechanical properties and biocorrosion behavior of Mg-0.8Mn-0.5Ca (wt. %) alloy was investigated. The major conclusions can be summarized as follows:

(1) The simulation of AEB process showed that the average effective plastic strain per pass for channels with the internal angle of 120° is about 1.93. This value was nearly 2 times of the average effective plastic strain reported for one pass of conventional ECAP.

(2) The average grain size was dramatically decreased from about 448.3 μm for the homogenized (starting) alloy to 1.55 μm for the three passes of deformation. Microstructural observations suggested a combination of continuous, discontinuous and twinning-induced dynamic recrystallization as the major mechanisms responsible for the observed grain refinement.

(3) Tensile and compressive strengths after three passes of AEB showed 2 and 1.5 times improvements due to considerable decrease in the average grain size, respectively.

(4) Tensile elongation decreased from 26 % for the homogenized sample to 7.5 % after three passes of ABE process due to the severe work-hardening, non-uniform strain and inhomogenies microstructure.

(5) Corrosion resistance increased from 1.1 to 14.159 $K\Omega\, Cm^2$ after three passes of ABE. Grain refinement by AEB resulted in the formation of hydroxyapatite layer with a more uniform distribution on the grain boundaries. The hydroxyapatite layer imparted better corrosion resistance to the AEBed samples.

References

[1] N. Li, Y. Zheng, J. Mater. Sci. Technol., 29 (6) (2013) 489-502.

[2] S. Hiromoto, T. Shishido, A. Yamamoto, N. Maruyama, H. Somekawa, T. Mukai. Corr. Sci., 50 (10) (2008) 2906-2913.

[3] H. Ibrahim, N. Moghaddam, M. Elahinia. Metall. Mater. Eng. 1 (2017) 1-7.

[4] H. Bakhsheshi-Rad, M. Idris, M. Abdul-Kadir, A. Ourdjini, M. Medraj, M. Daroonparvar. Mater. Des. 53 (2014) 283-292.

[5] R. Lapovok, P.F. Thomson, R. Cottam, Y. Estrin. J. Mater. Sci., 40 (7) (2005) 1699-1708.

[6] H. Miura, T. Maruoka, X. Yang, and J. J. Jonas. Scr. Mater., 66 (1) (2012) 49-51.

[7] R.B. Figueiredo, T.G. Langdon. J. Mater. Sci ., 45 (17) (2010) 4827-4836.

[8] S.K. Asl, S. Nemeth, M.J. Tan. Surf. Coat. Tech., 258 (2014) 931-937.

[9] X.N. Gu, N. Li, W.R. Zhou, Y.F. Zheng, X. Zhao, Q.Z. Cai, L. Ruan. Acta Biomater., 7 (4) (2011) 1880-1889.

[10] H.X. Wang, S.K. Guan, X. Wang, C.X. Ren, L.G. Wang. Acta. Biomater., 6 (5) (2010) 1743-1748.

[11] S. Agarwal, J. Curtin, B. Duffy, S. Jaiswal. Mater. Sci. Eng. C., 68 (2016) 948-963.

[12] J. Fan, X. Qiu, X. Niu, Z. Tian, W. Sun, X. Liu, Y. Li, W. Li. J. Meng, Mater. Sci. Eng. C., 33 (4) (2013) 2345-2352.

[13] T. Lei, W. Tang, S.H. Cai, F.F. Feng, N.F. Li. Corr. Sci., 54 (2012) 270-277.

[14] M.C. Turhan, Q. Li, H. Jha, R.F. Singer, S. Virtanen. Electrochim. Acta., 56 (20) (2011) 7141-7148.

[15] E.C. Meng, S.K. Guan, H.X. Wang, L.G. Wang. S.J. Zhu, J.H. Hu, C.X. Ren, J.H. Gao, Y.S. Feng. Appl. Surf. Sci., 257(11) (2011) 4811-4816.

[16] D.Orlov, G. Raab, T.T. Lamark, M. Popov, Y. Estrin. Acta. Mater., 59 (15) (2011) 375-385.

[17] X.N. Gu, Y.F. Zheng, Y. Cheng, S.P. Zhong, T.F. Xi. Biomater., 30 (4) (2009) 484-498.

[18] R. Radha, D. Sreekanth. J. Mag. Alloy., 5(3) (2017) 286-312.

[19] M. Kaviani, G.R. Ebrahimi, H.R. Ezatpour, Mater. Hem. Phys. 234 (2019) 245-258.

[20] B.S. Padekar, R.K. Singh Raman, V.S. Raja, L. Paul, Corros. Sci. 71 (2013) 1-9.

[21] H.Y. Ha, H.J. Kim, S.M. Baek, S.D. Sohn, H.J. Shin, H.Y. Jeong, S.H. Park, C.D. Yim, B.S. You, J.G. Lee, S.S. Park. Scr. Mater., 109 (2015) 38-43.

[22] Y. Ding, C. Wen, P. Hodgson, Y. Li. J. Mater. Chem. B., 2(14) (2014) 1912-1933.

[23] Y. Ali, D. Qiu, B. Jiang, F. Pan, M.X. Zhang. J. Alloys Compd., 619 (2015) 639-651.

[24] F. Zhang, A. Ma, D. Song, J. Jiang, F. Lu, L. Zhang, D. Yang, J. Chen. J. Rare Earths., 33 (1) (2015) 93-101.

[25] S.Z. Khalajabadi, N. Ahmad, A. Yahya, M.A. Yajid., A. Samavati, S. Asadi, A. Arafat, M.R. Kadir. Ceram. Int., 42(16) (2016) 18223-18237.

[26] X. Wang, P. Zhang, L.H. Dong, X.L. Ma, J.T. Li, Y.F. Zheng. Mater. Des., 54 (2014) 995-1001.

[27] M. Razavi, M.H. Fathi, M. Meratian. Mater. Lett., 64 (22) (2010) 2487-2490.

[28] H. Wang, S. Guan, Y. Wang, H. Liu, H. Wang, L. Wang, C. Ren, S. Zhu, K. Chen. Colloids. Surf. B: Biointerfaces., 88 (1) (2011) 254-259.

[29] M. Li, Y. Cheng, Y.F. Zheng, X. Zhang, T.F. Xi, S.C. Wei. Surf. Coat. Tech., 228 (2013) 262-265.

[30] E.C. Meng, S.K. Guan, H.X. Wang, L.G. Wang, S.J. Zhu, J.H. Hu, C.X. Ren, J.H. Gao, Y.S. Feng. Surf. Sci., 257 (11) (2011) 4811-4816.

[31] R. Del Campo, B. Savoini, A. Munoz, M. A. Monge, R. Pareja. J. Mech. Behav. Biomed. Mater., 69 (2017) 135-143.

[32] Y. Huang, D. Liu, L. Anguilano, C. You, M. Chen. Mater. Sci. Eng. C., 54 (2015) 120-132.

[33] K.B. Nie, K.K. Deng, X.J. Wang, T.Wang, K. Wu. Mater. Charact., 124 (2017) 14.

[34] S. Rusza, O. Hilšer, V. Ochodek , L. Čížek, M. Kraus, V. Mareš, A. Grajcar, J. Švec, J. Min. Metall. Sect. B-Metall., 56 (2) B (2020) 161-170.

[35] G.K. Manjunath, K. Udaya Bhat, G.V. Preetham Kumar, M R. Ramesh, Trans. Indian Inst. Met. 71 (2018) 1919-1931.

[36] H.K. Kim. Mater. Sci. Eng. A., 515 (1-2) (2009) 66-70.

[37] S. M. Masoudpanah, R. Mahmudi. Mater. Des., 31 (7) (2010) 3512-3517.

[38] P. Bernard, S. Bag, K. Huang, R.E. Logé. Mater. Sci. Eng. A., 528 (24) (2011) 7357-7367.

[39] D.G. Cram, H.S. Zurob, Y.J.M. Brechet, C.R.A. Hutchinson. Acta. Mater., 57 (17) (2009) 5218-5228.

[40] F. Montheillet, O. Lurdos, G. Damamme. Acta. Mater., 57 (5) (2009) 1602-1612.

[41] F.J. Humphreys, M. hatherly, Recrystallization and Related Annealing Phenomena, second ed., Oxford, Pergamon, New York, (2004) 252.

[42] A. Yamashita, Z. Horita, T.G. Langdon. Mater. Sci. Eng. A., 300 (2001) 142-147.

[43] M. Kavyani, G.R. Ebrahimi, H.R. Ezatpour, M. Jahazi. J. Mag. Alloys., (2021).

[44] Q. Ma, B. Li, E.B. Marin, S.J. Horstemeyer, Scr. Mater. 65 (9) (2011) 823-826.

[45] P. C. Wu, C. P. Chang, P. W. Kao. Mater. Sci. Eng. A., 374 (1-2) (2004) 196-203.

[46] G. A. Malygin. Phys. Solid. State. 48 (2006) 693–699.

[47] X. Luo, Z. Feng, T. Yu, T. Huang, R. Li, G. Wu, N. Hansen, X. Huang. Mater. Sci. Eng. A., 772 (2020) 138763.

[48] L.Hou, T, Wang, R. Wu, J. Zhang, M. Zhang, A. Dong, B. Sun, S. Betsofen, B. Krit. Mater. Sci. Technol., 34 (2018) 317-323.

[49] S. Amirkhanlou, M. Ketabchi, N. Parvin, S. Khorsand, R. Bahrami. Mater. Des., 51 (2013) 367.

[50] E.A. El-Danaf, M.S. Soliman, A.A. Almajid, M.M. El-Rayes. Mater. Sci. Eng. A. 458 (2007) 226–34.

[51] L. Olejnik, A. Rosochowski. Tech. Sci., 53 (2005) (4) 53.

[52] M. Eizadjou, H. D. Manesh, K. Janghorban. Mater Des., 30 (10) (2009) 4156-4146.

[53] R.B. Figueiredo, T.G. Langdon. Journal of materials science. Mater. Sci. Eng. A., 501 (2009) 105-114.

[54] K. Máthis, J. Gubicza, N.H. Nam. J. Alloys. Compd., 394 (2005) 194-199.

[55] P. Klimanek, A. Pötzsch. Mater. Sci. Eng. A., 324 (1-2) (2002) 145-150.

[56] C. W. Su, L. Lu, M. O. Lai. Mater. Sci. Eng. A. 434 (1-2) (2006) 227-236.

[57] L. Jin, D. Lin, D. Mao, X. Zeng, B. Chen, W. Ding. Mater. Sci. Eng. A., 423 (1-2) (2006) 247-252.

[58] F. Witte, F. Feyerabend, P. Maier, J. Fischer, M. Störmer, C. Blawert, W. Dietzel, N. Hort, Biomater. 28(13) (2007) 2163-2174.

[59] X. Zhang, G. Yuan, J. Niu, P. Fu, W. Ding, J. Mech. Behav. Biomed. Mater. 9 (2012) 153-162.

[60] L.B. Tong, J.H. Chu, W.T. Sun, Z.H. Jiang, D.N. Zou, K.S. Wang, S. Kamado, M.Y. Zheng, J. Alloys Compd. 825 (2020) 153942.

[61] H.R. Ezatpour, S.A Sajjadi, M.H. Sabzevar, Y.Z. Huang. Mater. Sci. Eng. A. 607 (2014) 589-595.

[62] C. Zhang, S. Guan, L. Wang, S. Zhu, L. Chang. J. Mater. Res. 32(6) (2017) 1061-72.

[63] F. Zhang, M. Aibin, S. Dan, J. Jiang, L. Fumin, L. Zhang. J. Rare Earth, 33 (2015) 93-101.

[64] X. Zhang, Z. Wang, G. Yuan, Y. Xue. Mater. Sci. Eng. B. 177(3) (2012) 1113-9.

[65] D. Song, G. Guo, J. Jiang, L. Zhang, A. Ma, X. Ma. Prog. Natural Sci: Mater. Int. 26(6) (2016) 590-9.

[66] X. Lin, L. Tan, Q. Zhang, K. Yang, Z. Hu, J. Qiu. Acta Biomater, 9(10) (2013) 8631-42.

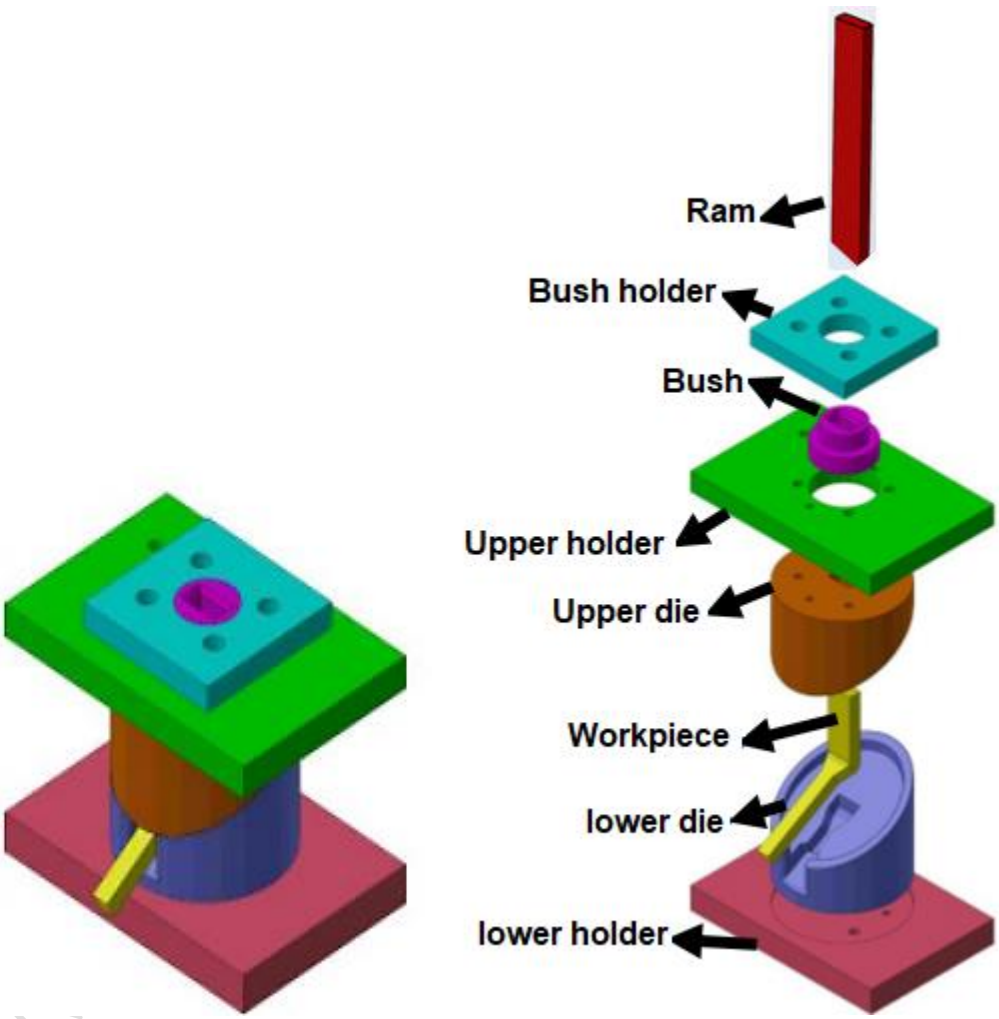

Fig. 1. Schematic illustration of ABE set up.

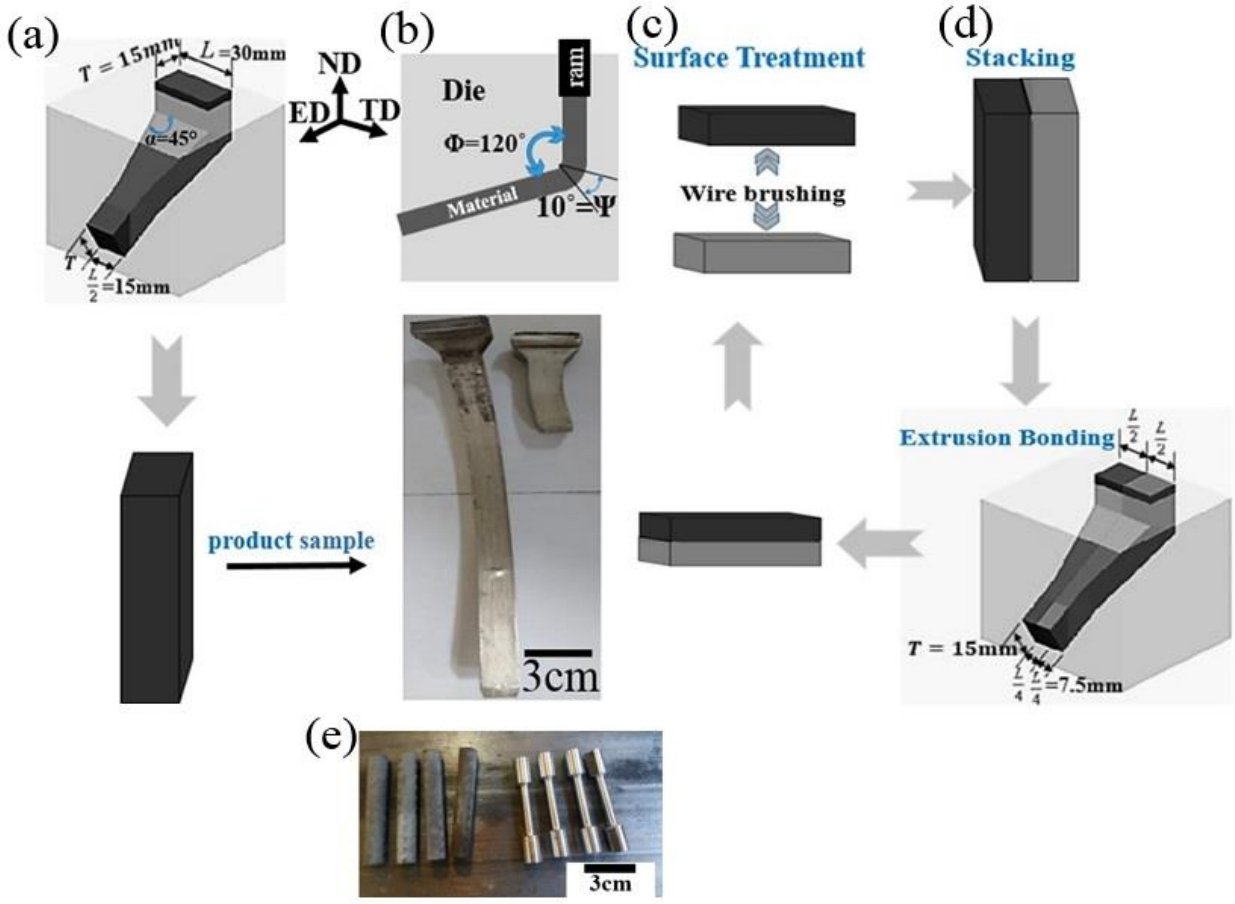

Fig. 2. Schematics of the die dimensions and sample feeding in the accumulative extrusion bonding (AEB) using 120°-angle channels process at first pass, (a) the die cross section, (b) the inside and outside angles of intersection between the entry and exit channels, (c) wire brushing and (d) second and third passes.

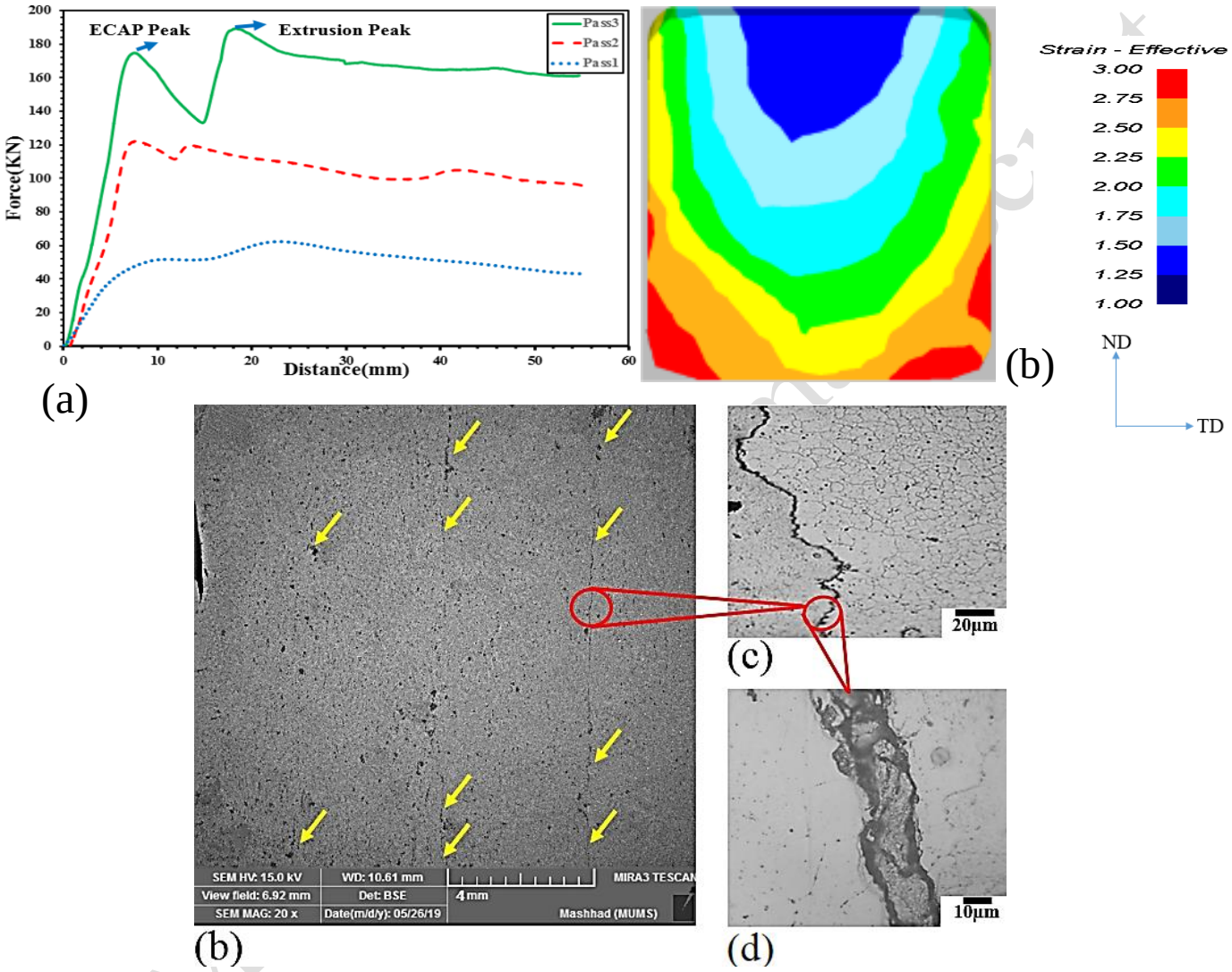

Fig. 3. (a) The force-displacement plots of ABEed samples at different passes, (b) the distribution and amount of average effective plastic strain in channels with 120 angle (φ), SEM micrograph showing the layers joint by AEB and (c, d) morphology of layers interface in two magnifications.

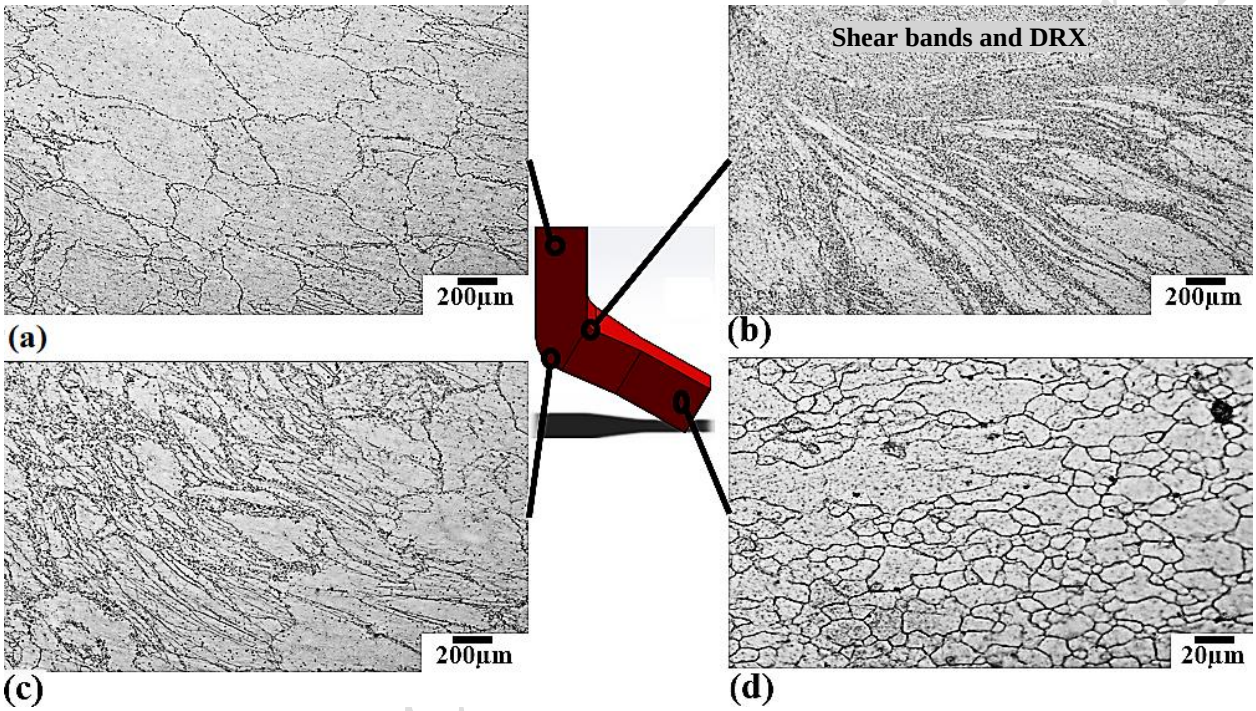

Fig. 4. Optical micrographs displaying the microstructures of Mg-0.8Mn-0.5Ca alloy after one-pass of AEB: (a) at the starting point (homogenized alloy), (b, c) the top and bottom of ECAP region, and (d) after ECAP and extrusion.

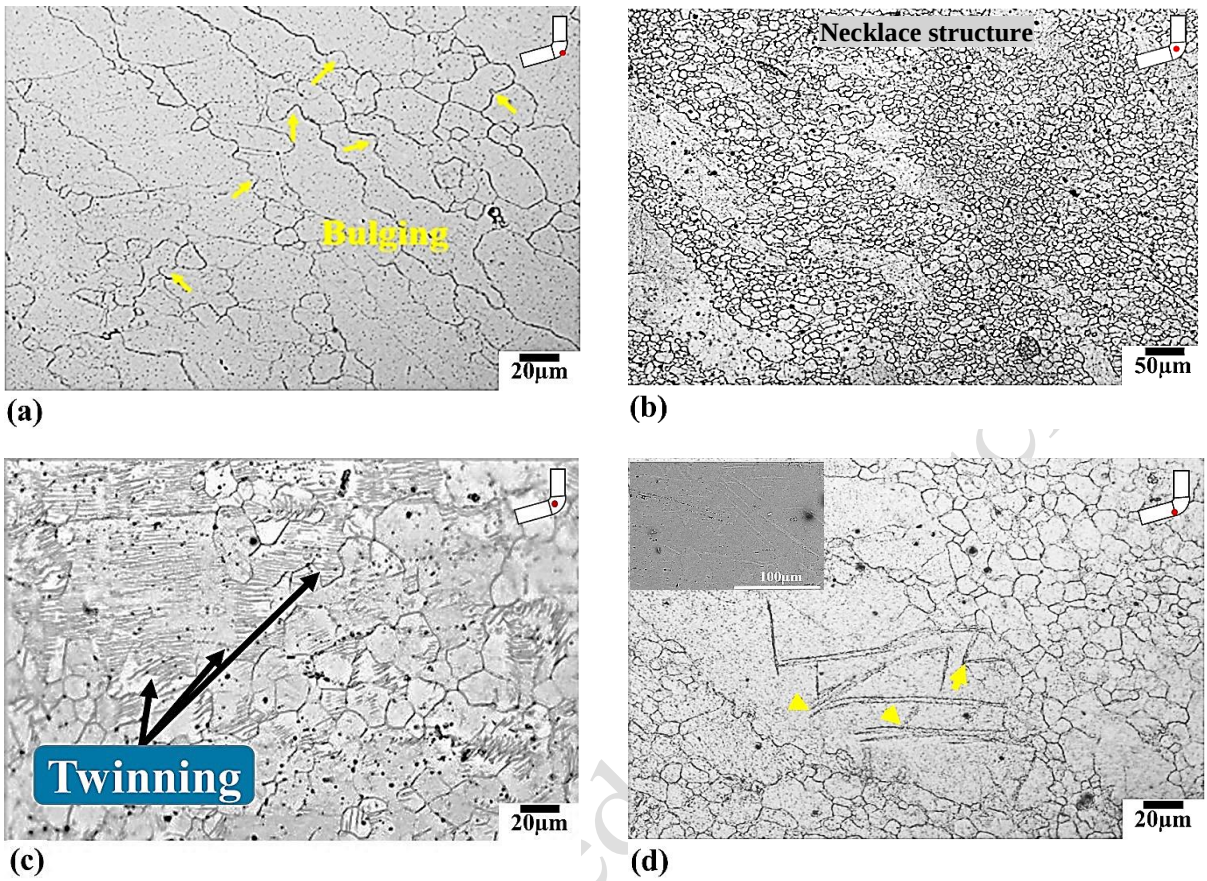

Fig. 5. Optical micrographs showing the (a) the grain boundary bulging in the lower part of ECAP region, (b) the necklace structure in the middle of ECAP region, (c) the formation of twin boundaries and their role on the recrystallization of Mg-0.8Mn-0.5Ca after one-pass of AEB and (d) in the middle and after of ECAP region, respectively (the inset in (d) shows the SEM image of twin boundaries in the ECAP region).

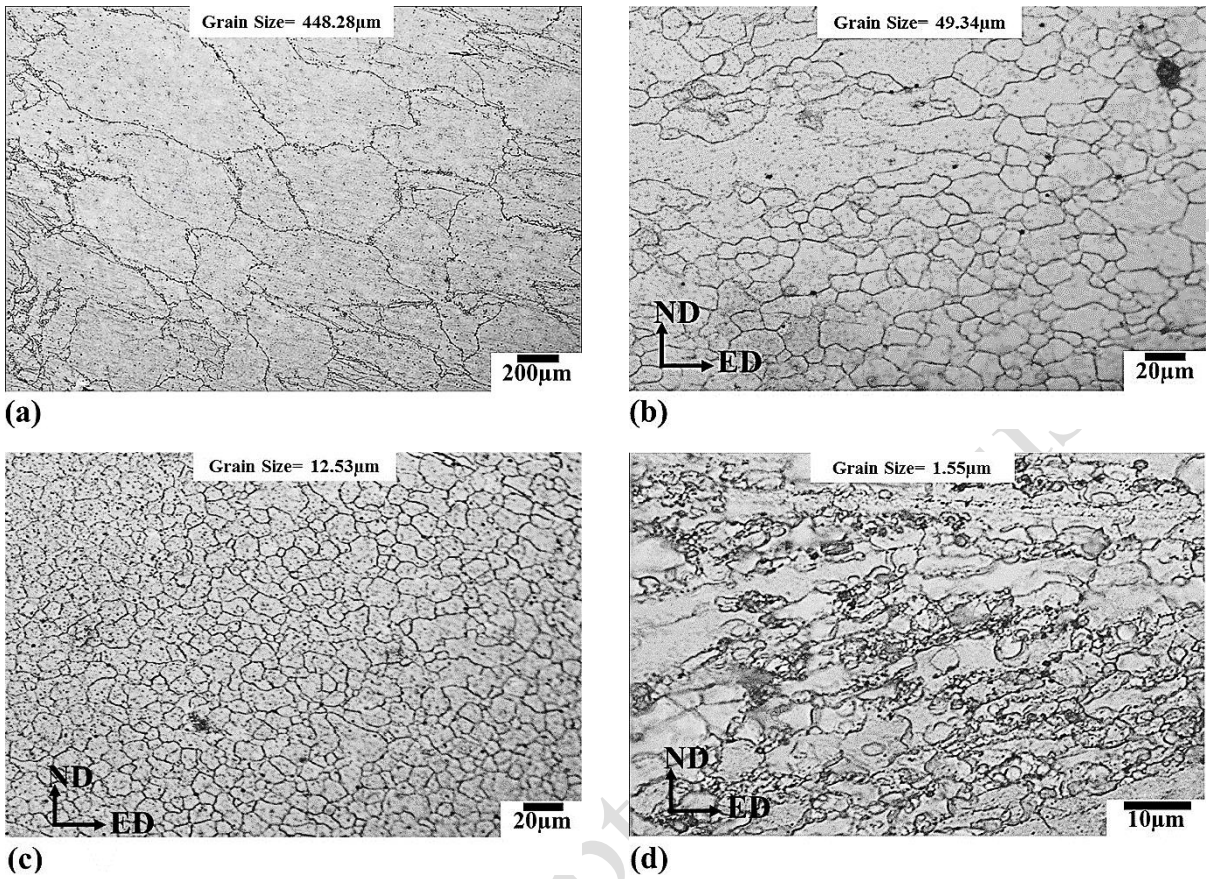

Fig. 6. Optical micrographs of the samples at different conditions; (a) homogenized, (b) after the first pass, (c) after the second pass and (d) after the third pass ABE process.

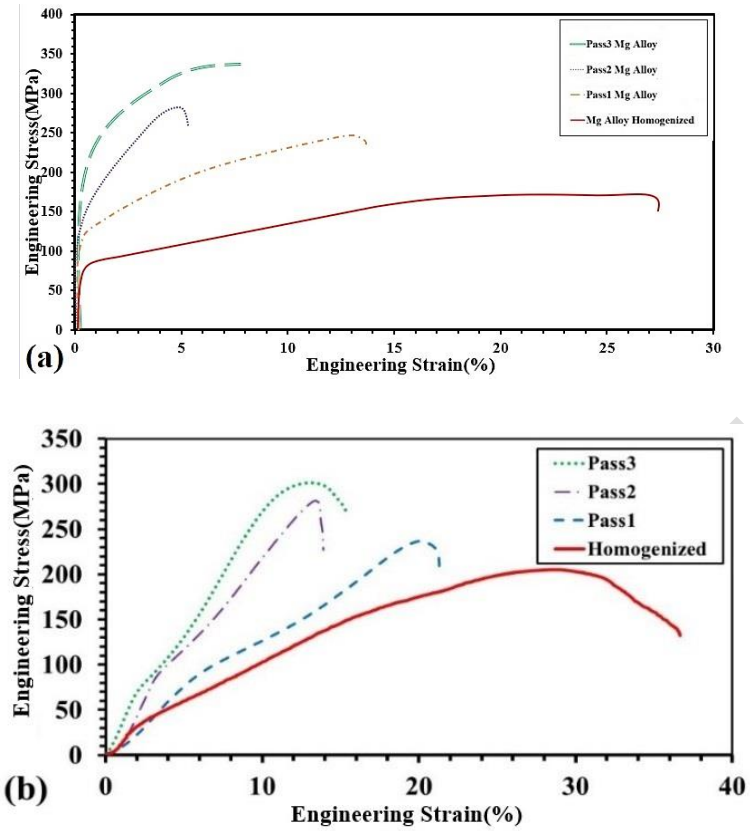

Fig. 7. (a) Tensile and (b) compressive stress-strain curves of the homogenized and AEBed samples.

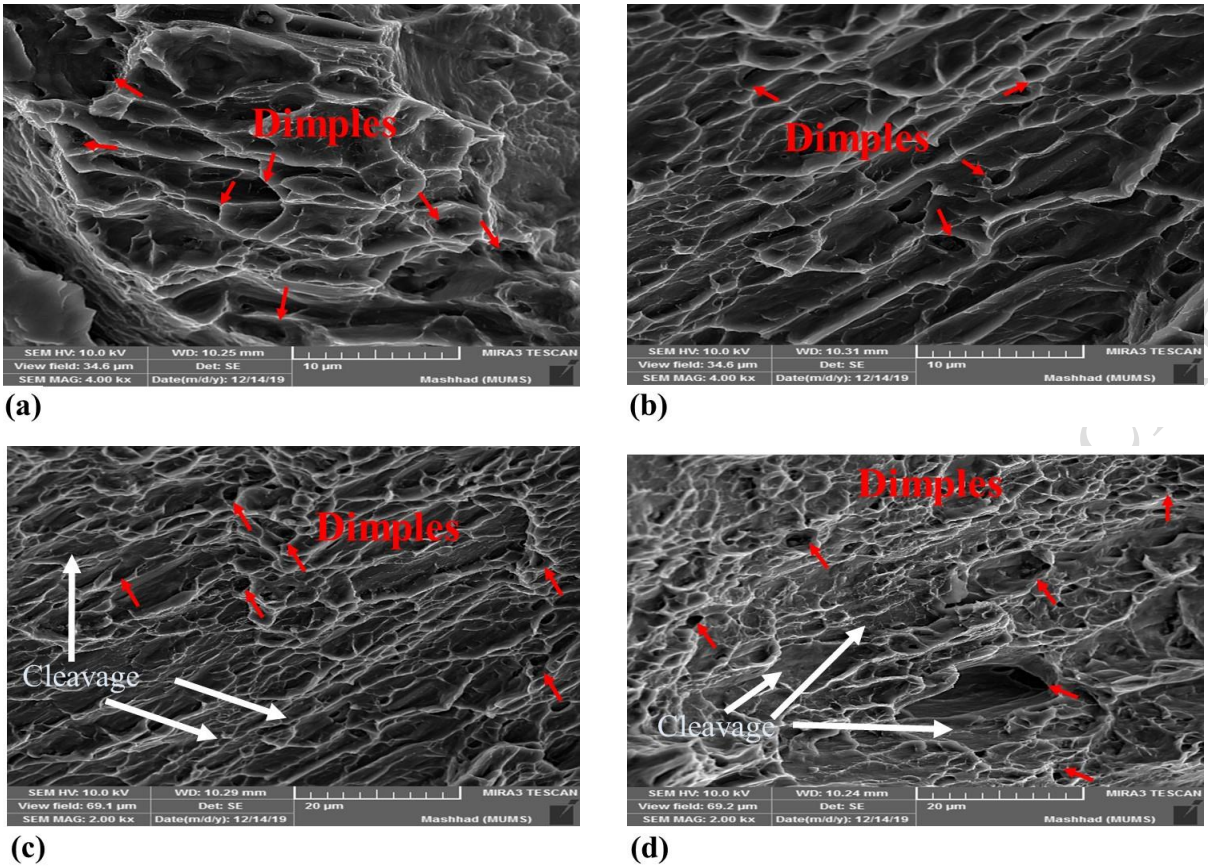

Fig. 8. SEM micrographs showing the fractured surfaces of the samples at different conditions of (a) homogenized, (b) 1-pass, (c) 2-pass and (d) 3-pass ABE process.

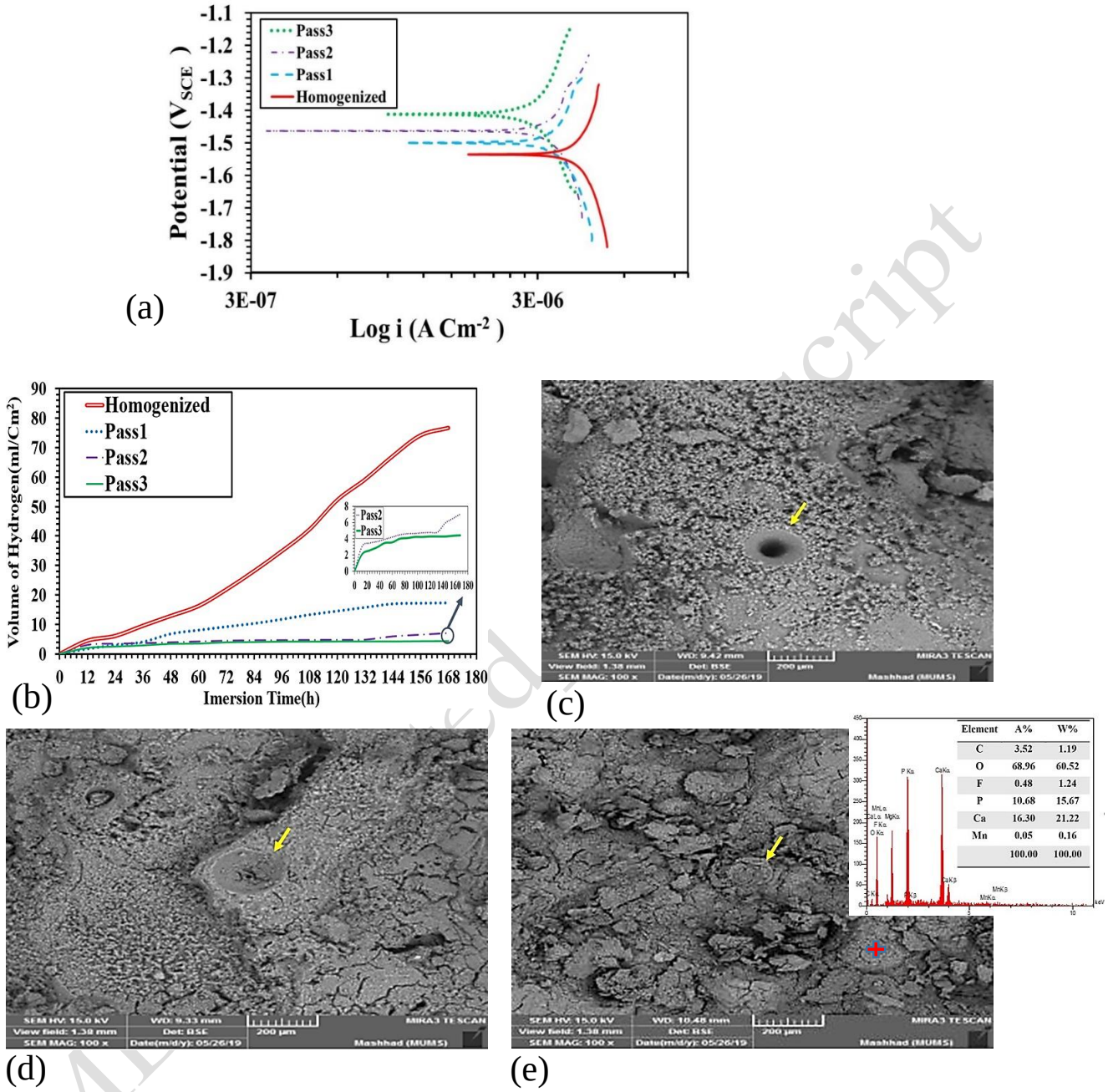

Fig. 9. (a) PDP test diagrams, (b) hydrogen evolution diagrams, FESEM micrographs from the samples subjected to HE test at different conditions of (c) homogenized, (d) 1-pass and (e) 3-pass ABE process.